Research Article | Vol. 33, No. 25 / 15 Dec 2025 / Optics Express 53268
Optics EXPRESS

Nonlinear refractive index measurements of solids and the impact of B-integral on the phase of generated high-order harmonics

ROY VAN DER LINDEN,[1] NATALIIA KUZKOVA,[1,2] AND PETER M. KRAUS[1,2,*]

[1]Advanced Research Center for Nanolithography, Science Park 106, 1098 XG Amsterdam, The Netherlands
[2]LaserLaB, Department of Physics and Astronomy, Vrije Universiteit, De Boelelaan 1105, 1081 HV Amsterdam, The Netherlands
[*]p.kraus@arcnl.nl

Abstract: We present an interferometric method that employs a birefringent common-path interferometer to measure absolute nonlinear refractive indices in 5 mm thick CaF_2, SiO_2, NBK-7 and KBr for femtosecond pulses at 804 nm center wavelength. The measured nonlinear refractive indices are found to be in agreement with previous literature, over a broad range of pulse energies. In addition, we show and highlight the importance of thorough B-integral characterization when using this birefringent common-path interferometer for high-harmonic generation driven extreme-ultraviolet interferometry. The accumulated third-order nonlinear phase is shown to have significant impact on the harmonic phase after up-conversion to higher orders, but can be accounted for if correctly characterized.

1. Introduction

Within optical science, interferometry is a cornerstone of scientific advancement in active fields such as attosecond science [1], imaging [2] and gravitational wave detection [3]. While Mach-Zehnder and Michelson interferometers induce time delay between a reference and sample beam of light by splitting and geometrically altering their relative path lengths [4,5], common-path interferometers have the reference and sample beam follow the same or opposite paths [6,7]. This class of interferometers suffer significantly less from any undesired path length shifts due to beam pointing instability, mechanical vibrations of optics or air currents as both beams will be affected equally [8,9]. Birefringent common-path interferometers uniquely use the distinct refractive indices between orthogonal polarization components in a birefringent material to introduce retardation between the two beams [10]. In 2012, Brida et al. introduced the Translating-Wedge-Based Identical Pulses eNcoding System (TWINS), a birefringent common-path interferometer that parts two identical phase-locked pulse copies in time. Through spectral interferometry they confirmed the extremely high stability of the common-path configuration, with fixed delay fluctuations of only 5 as over 30 min and minimal time delay steps of 3.6 as. TWINS has since been used for Fourier transform spectroscopy in the extreme ultraviolet (XUV) [11], visible [12] and infrared [13] regions, as well as for hyperspectral imaging [14], and most recently in valleytronics [15], photocurrent spectroscopy [16] and XUV interferometry. The latter has been performed by seeding a XUV free-electron laser with UV pulse pairs from TWINS [17], as well as using near infrared (NIR) pulse pairs from TWINS to drive high-harmonic generation (HHG) by spatially separating foci of the two NIR beams in the HHG target.[11,18,19]. Lu et al. [18] and Kuzkova et al. [19] showed that the emission phase of XUV harmonics from solids depends on the relative intensities of the driver NIR pulse pair, confirming the intensity dependence of the

#579736 https://doi.org/10.1364/OE.579736
Journal © 2025 Received 22 Sep 2025; revised 6 Nov 2025; accepted 26 Nov 2025; published 10 Dec 2025

Optics EXPRESS

emission phase (dipole phase) of HHG. However, because HHG in solids requires intense peak intensities (several TW/cm^2), the two NIR beams additionally accumulate a nonlinear phase shift caused by the nonlinear refractive index n_2 of the transmissive optics within and beyond the TWINS and throughout propagation in the HHG target. Therefore, TWINS experiments that utilize pulse pairs of unequal intensities should carefully characterize the nonlinear phase that is accumulated and correct the experimental results for it. Such a correction was performed by Kuzkova et al. [19] for extracting the dipole phase of high-harmonic emission from solids in a TWINS-based interferometry measurement. Here we systematically extend the method to actually characterize the nonlinear phase accumulation and highlight its impact on measurements.

The XUV interferometry measurement [19] opened a pathway for a novel, compact and highly stable interferometric measurement technique of n_2. For parametric and instantaneous light-matter interactions, where the applied electric fields E are not too large ($\sim$ TW/cm^2), the field-induced polarization can be reasonably expanded using a Taylor series. The nonlinear refractive index n_2 arises from a third order term, given by $P^{(3)} = 3\epsilon_0 \sum_{jkl} \chi^{(3)}_{ijkl}(\omega;\omega,\omega,-\omega)E_j(\omega)E_k(\omega)E^*_l(\omega)$ [20]. This nonlinear polarization describes the interaction of three waves, twice of the fundamental frequency ω and one of $-\omega$. For isotropic media and parallel linearly polarized light, the nonlinear susceptibility $\chi^{(3)}_{ijkl}$ only has one independent element, $\chi^{(3)}_{1111}$. For a given wavelength λ, the effective refractive index $\tilde{n}$ then becomes,

$$\tilde{n}(\mathbf{r},t) = n_0 + n_2 I(\mathbf{r},t). \tag{1}$$

Here, $n_2 = 3\chi^{(3)}/(4n_0^2\epsilon_0 c)$, where c is the speed of light and n_0 is the refractive index due to the linear part of the polarization. Note that the intensity $I(\mathbf{r},t)$, and thus also $\tilde{n}(\mathbf{r},t)$, can vary spatially and temporally. The B-integral can then be defined, which describes the total nonlinear phase accumulated along the full propagation length throughout the medium,

$$B = \frac{2\pi}{\lambda}\int n_2 I(z)dz, \tag{2}$$

where z is the propagation distance. In the case where the intensity stays constant, the integral simplifies to $B = 2\pi/\lambda n_2 IL$, where L is the total propagation distance throughout the material.

Over the past few decades, n_2 has garnered special interest for applications like nonlinear pulse compression [21], optical limiting [22], and for many all-optical switching devices, such as fiber Bragg gratings [23,24], which have been used in all-optical logic gates [25,26], fiber couplers, and Sagnac interferometers. These applications require accurate n_2 characterization as to achieve sufficient nonlinearities while preventing medium damage from applying too high intensities.

Currently, n_2 databases heavily rely on Z-scan measurements, a method that exploits self-focusing, resulting from the radially varying intensity, to extract the real and imaginary parts of n_2 by scanning the focus through a sample. However, the accuracy of this method is limited by uncertainties in the beam quality factor, which rarely goes below 15% [27]. Other n_2 measurement techniques include (degenerate) four-wave mixing [28], nonlinear ellipse rotation [29,30], beam self-bending [31], third harmonic generation [32,33], two-beam coupling [34] and interferometric methods [35–37]. Jansonas et al. used the radial intensity dependence of a Gaussian beam to induce a radially dependent phase shift between a sample and reference arm, in a Mach-Zhender interferometer, to extract n_2.

Here we show that common-path interferometry can expand on the interferometric approaches and is able to measure absolute n_2 of solid media, the results of which agree with other techniques often utilized, such as the Z-scan. Furthermore, the uncertainties in our TWINS measurements of n_2 are likely on par with previously demonstrated methods (to the extent that uncertainties and definitions thereof are provided). Lastly, we demonstrate that accurate B-integral characterization is crucial for TWINS-driven HHG XUV interferometry, as the nonlinear phase accumulated during propagation, within and before the target, is multiplied during the high-order harmonic up-conversion.

Optics EXPRESS

2. Methods

A schematic layout of the experimental setup is presented in Fig. 1(a). A Ti:sapphire laser amplifier system (Astrella, Coherent) delivers pulses centered at 804 nm, with 7 mJ pulse energy, 40 fs full width at half maximum (FWHM) pulse duration, and a repetition rate of 1 kHz. Before entering the setup, the laser output was attenuated to tens of μJ using a half-wave plate and polarizer. After the attenuation, a second half-wave plate, installed on a motorized rotating mount, was positioned in front of the interferometer to control the input laser polarization. The beam is restricted by an aperture before the TWINS, due to the limited size of the optics.

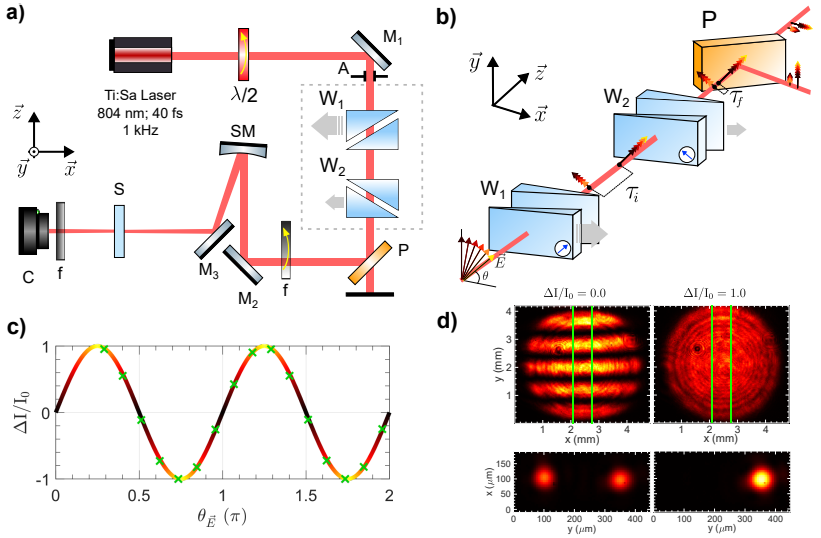

Fig. 1. (a) Schematic overview of the experimental setup, consisting of the following optics: mirror (M_i), half-wave plate ($\lambda/2$) in a rotational mount (indicated by the yellow arrow), aperture (A), pair of wedges (W_i), polarizer (P), spherical mirror (SM), sample (S), filter (f) and a CMOS camera (C). (b) TWINS interferometer, blue arrows on the wedges indicate the optical axis. Input polarization direction is shown varying from 0 to 45° from black to yellow respectively. (c) Relative intensity change as function of input angle as defined in (b), green crosses show measured values. (d) Spatial beam profile as seen after (first row) and in (second row) focus for $\Delta I/I_0 = 0$ (first column) and $\Delta I/I_0 = 1$ (second column). The green lines indicate the summation range, as explained in the Methods section.

The TWINS interferometer consists of two pairs of birefringent wedges with opposite optical axes, see Fig. 1(b). Specifically, alpha barium borate (α-BBO) 20x20x1 mm birefringent wedges (United Crystals Inc.) with an apex angle $\alpha = 14°$ were used. The optical axes were under an angle of 45° from the 20 mm edges and the difference between the refractive indices of the extraordinary n_e and ordinary n_o axis was $\Delta n = n_e - n_o = 0.119$ at 800 nm. Starting with a s-polarized pulse, the first pair of wedges delays the polarization component along the extraordinary axis relative to the polarization component along the ordinary axis. The first wedge of pair W_1 is mounted on a manual stage, allowing control over the path length through the first pair of wedges and thus setting the initial relative time delay τ_i, which was held constant throughout the experiment. Thereafter, the two orthogonal polarized pulse copies go through a second pair of wedges with optical axes rotated with 90° relative to the first pair, compensating the large initial delay. The second wedge of W_2 is placed on a linear piezo stage, with a minimal step size of 1 nm, that can be translated in and out of the beam path. Given the stepsize, the apex angle and Δn, the TWINS interferometer allows for a final sub-attosecond delay τ_f between the two pulse copies.

Optics EXPRESS

However, for the n_2 characterization, as described later, also the final time delay was held fixed. In order for the two pulses to interfere, the s-polarization projections are taken from the reflection of a polarizer. The normalized intensity difference, defined as $\Delta I/I_0 = (I_1 - I_2)/(I_1 + I_2)$, with I_1 and I_2 corresponding to the peak intensity of first and second pulse and $I_0 = I_1 + I_2$, can be scanned by rotating the half-waveplate at the input of the interferometer, as shown in Fig. 1(c). The first wedge of W_2 is slightly tilted around the x-axis that, due to the varying refractive indices experienced by both pulses, introduces an angle (~0.5 mrad) between the k-vectors at the exit of the interferometer. The two phase-locked pulses are then steered onto and focused by an Ag-coated spherical mirror with a focal length of 50 cm. The beam profile in and out of focus are shown per column in Fig. 1(d) for $\Delta I/I_0 = 0$ and $\Delta I/I_0 = 1$. In focus ($z = 0$) the $1/e^2$ beam area A_i was measured to be $6.45 \cdot 10^3$ μm^2 and $6.73 \cdot 10^3$ μm^2 (corresponding to an effective beam radius of 45 μm and 46 μm) for pulse 1 and 2 respectively, see Fig. 2(c). The pulse separation is 247 μm. The small (~ 3%) difference in peak intensity shown in Fig. 2(c) means the measurement was not taken at exact $\Delta I/I_0 = 0.0$. Yet, this should not effect the beam area. For $z = \pm 3$ mm around the focus, the change in area, for both pulses, was less than 5%. The pulse duration τ_p before focus was measured using a home build second harmonic Frequency Resolved Optical Gating (FROG) to have a Gaussian FWHM of 47 ± 1 fs, see Fig. 2(a),(b). 5-mm thick uncoated Thorlabs isotropic windows were used as samples and placed orthogonal to the beam path at $z = 0$. As confirmed by the beam area measurements of $z = 0 \pm 3$ mm, the sample thickness was chosen to be smaller than the Rayleigh length. The focus position, with sample in, was calibrated by looking at the threshold of white light generation (WLG), thereafter the power was lowered below the WLG threshold. The sample position in focus, as determined by the WLG threshold, agreed with the position of the beam profiler in focus. Out of focus a Basler CMOS camera captured the interference pattern between the two pulse copies, as shown in the first row of Fig. 1(d). For each sample, the input polarization was scanned over 90°, going from $\Delta I/I_0 = 1$ (all intensity in the first pulse) to $\Delta I/I_0 = -1$ (all intensity in the second pulse). Figure 3(a) shows the projection of the interference pattern of the area bordered by the green vertical lines,

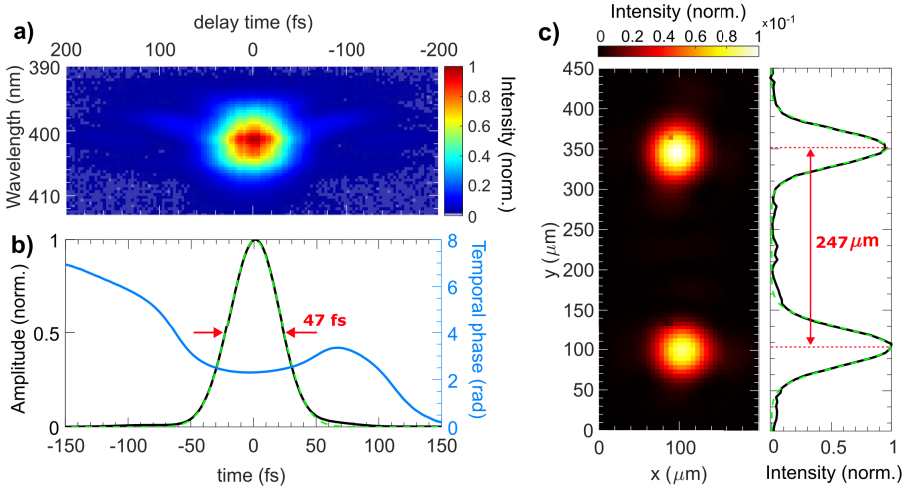

Fig. 2. (a) Measured FROG trace of the pulses before focusing. (b) Reconstructed electric field (solid black line) as a function of time of the measured FROG trace with it's temporal phase (solid blue line). The dashed green line shows a fitted Gaussian function where the red arrows indicate the corresponding FWHM of the fit. (c) Spatial beam profile measured in the focal plane. Right panel shows the summed intensity (solid black line) with two separately fitted Gaussians (dashed green line). Red arrow shows the foci separation.

Optics EXPRESS

as seen in Fig. 1(d), as function of the normalized intensity difference of the pulse pair. As the relative phase will dependent on the spatial intensity profile of the beam, exact peak locations were extracted via local Gaussian fits around the peak for every projected interference pattern, see Fig. 3(b). Figure 3(c) compares the linear fits of different sample for $I_0 = 55$ GW/cm^2. The fits were done for a range of $-0.67 \leq \Delta I/I_0 \leq 0.67$ where clear fringe contrast can be seen.

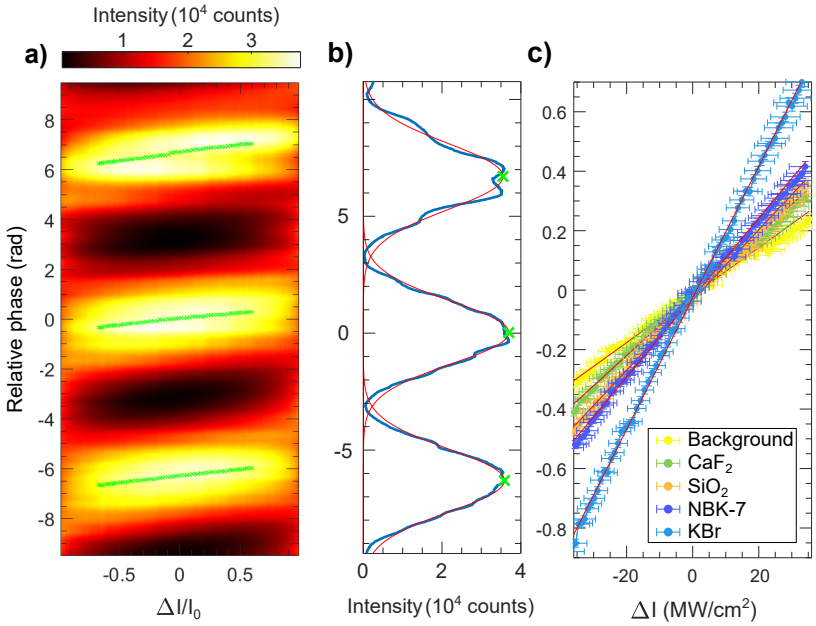

Fig. 3. (a) Projected interference pattern as function of the normalized intensity difference for SiO_2 for $I_0 = 24$ GW/cm^2. Green crosses show the fitted peaks. (b) The interference for $\Delta I/I_0 = 0$ of a). Red lines show the Gaussian fits per peak, with the green crosses indicating the maxima. (c) Comparison of the central fringe $\Delta I/I_0$ dependent relative phase of the samples measured for $I_0 = 55$ GW/cm^2, linear fits of the data is shown by the solid red lines. Error bars show the $\pm 2\sigma$ uncertainty. The slope is proportional to the nonlinear refractive index n_2.

In order to accurately extract n_2 from the observed linear relation, shown in Fig. 3(c) for different samples, the peak intensity must be measured or calibrated precisely. In this work, the peak intensity per pulse I_i was calculated using $I_i = 4\sqrt{\ln 2/\pi} \cdot r_i t_s E_p/(\tau_p A_i)$. Here, the prefactor accounts for the Gaussian pulse shape (see Fig. 2(b)) and $r_i = I_i/I_0$ is the intensity ratio between the two pulses. r_i was calibrated using beam profile measurements in the focal plane as function of $\Delta I/I_0$, taking into account any transmission or reflection difference due to varying polarization angles. t_s is the sample dependent transmission through the first surface and E_p the total pulse energy. For each parameter an accompanying uncertainty was measured. The uncertainty in the pulse duration is taken to be twice the uncertainty given by the FROG reconstruction. As the relative phase difference originates straight from the B-integral (Eq. (2)), the nonlinear refractive index can then be extracted using the following,

$$n_2 = a\frac{\lambda}{2\pi L}. \tag{3}$$

Here a is the slope taken from the linear fit, as seen in Fig. 3(c). The uncertainty of ΔI is calculated using error propagation of the uncertainties of all the measured parameters used to calculate the pulse intensities. Uncertainty in the fitted peak locations of the relative phase are

Optics EXPRESS

also plotted, yet not visible due to their low contributions. Both uncertainty in ΔI and relative phase position of the fringes were used to find an uncertainty of the slope a [38].

3. Results and discussion

3.1. Nonlinear refractive index and phase characterization in the near-infrared

To demonstrate the use of TWINS as an absolute n_2 measurement tool, four common substrate materials Ca_2, SiO_2, NBK-7 and KBr, were chosen as samples to test the procedure described above. Per sample, n_2 was calculated from the measured relative phase shift, according to Eq. (3), for six input peak intensities, ranging from 24 to 55 GW/cm^2, see Fig. 4. For every intensity a background relative phase shift was measured without sample and subtracted from the sample data to account for the B-integral accumulated anywhere else along the beam path as well as any other linear phase changes that might occur. As the n_2 of air is three orders of magnitude lower [39] than that of the samples measured, the B-integral contribution of the focused spot in air during the background measurement is within our final uncertainty and can be neglected. As shown in Fig. 4, no trend between input peak intensity and extracted n_2 was observed. Thus it can be concluded that self-focusing or other higher-order nonlinear effects were not significant in the chosen measurement conditions. In addition, the transmission of every sample remained constant over the full intensity range and agreed well with the values reported by the supplier, thereby giving no indication of nonlinear absorption.

The n_2 results (averaged over all intensities), as well as comparison to existing literature values from Z-scans, are summarized in Table 1. All reported TWINS values are taken only from the central fringe, see Fig. 3, that correspond to the peak of the far-field gaussian spatial intensity profile, such that, together with the summation range shown in Fig. 1, only the highest intensity region is selected.

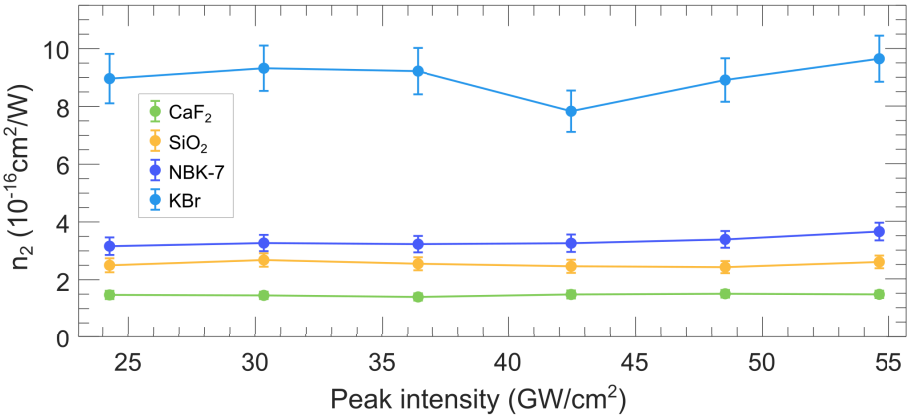

Fig. 4. Measured n_2 as function of input intensities. The error bars denote the $\pm 2\sigma$ uncertainty. All shown n_2 are taken from the central fringe in Fig. 3.

To verify the methodology, the experiments were simulated using Fourier optics [40]: two beams of equal size and tilt as experimentally measured were propagated through an iris and focused to the focal plane. Here, each beam was given a phase profile given by the B-integral, with nonlinear refractive indices, n_2^{in}, that were chosen to match literature data [27,41] of the materials used in the experiments. The applied intensities, wavelength, and sample thickness matched those used in the experiments. Both beams were then propagated to the camera plane where the experimental methodology was applied to extract an output nonlinear refractive index,

Optics EXPRESS

Table 1. Measured values of n_2 compared to literature values for four samples

Sample	n_2 / 10^{-16} (cm^2/W)	Wavelength (nm)	Method	Ref.
CaF_2	1.47 ± 0.26	800	TWINS	This work
	1.8 ± 0.27	800	Z-scan	[27]
SiO_2	2.54 ± 0.45	800	TWINS	This work
	2.7 ± 0.41	800	Z-scan	[27]
NBK-7	3.33 ± 0.59	800	TWINS	This work
	3.3 ± 0.50	800	Z-scan	[27]
KBr	8.98 ± 1.58	800	TWINS	This work
	7.87 ± 1.62	1064	Z-scan	[41]

Uncertainties of the reported values from this work are defined as $\pm 2\sigma$. As for the references, no explicit definition was given regarding the uncertainties.

n_2^{out}. Results of the simulations unveiled that the relative phase shift measured at the camera plane is systematically lower than what is applied in focus due to coupling between different amplitude and phase components of the near- and far-field. This caused n_2^{out} to be lower than what was applied in focus, namely $n_2^{in}/n_2^{out} = 1.9$. Additionally, as shown in Fig. 2, the pulses have a temporally Gaussian intensity profile. Due to the slow response time of the camera, the captured data will be a weighted average of the temporal intensity profile that also lowers the measured n_2. Comparing simulations of a pulse with a flat top intensity profile in time with a Gaussian intensity profile showed an additional factor of $n_2^{out,FT}/n_2^{out,G} = 1.4$. Both factors are taken into account for the final n_2, as presented in Fig. 4 and outlined in Table 1.

All n_2 of the measured samples using the TWINS common-path interferometry technique overlap, within uncertainty, with values reported by Z-scans. The uncertainties of the TWINS method are slightly higher for SiO_2 and NBK-7 (assuming that the reported Z-scans were defined as $\geq 2\sigma$). However, no correlation between uncertainty in I_1 and I_2 was assumed, which due to the common-path interferometric nature of the setup, makes the given uncertainty an upper bound. In general, the uncertainty of the current technique could be improved with high accuracy intensity calibration, finer wave plate step sizes and spatial cleaning of the intensity profile. The latter would benefit the uncertainty in the y-axis direction of Fig. 3(c), however, as it is, the Gaussian fitting of the central fringe already provided R-squared values of >0.98. The major part of the uncertainty comes from the uncertainty in the intensity calibration (x-axis of Fig. 3(c)), which remains a bottleneck for most of n_2 measurement techniques.

3.2. Nonlinear phase effects on high-harmonic driven XUV interferometry

Due to its high long-term stability, TWINS interferometry has been performed over many broad spectral regions. To highlight the importance of B-integral characterization when using TWINS, Fig. 5 shows an XUV interferometry measurement performed with the same common-path interferometer as described in the Methods section. However, instead of placing a mirror after the focusing optic to steer the foci into a solid sample, the pulse replicas propagate to their focal plane in a gas cell, housed inside a vacuum chamber. Using high peak intensities (~100 TW/cm^2), the highly nonlinear interaction between the gas medium and the laser pulses generate high-order harmonics in the XUV. Thereafter, the harmonics spatially overlap and interfere in the far-field, where they are detected by a XUV spectrometer, consisting of an unequally spaced curved-groove laminar-type replica XUV grating with 1200 lines/mm, a double-stack microchannel plate detector with phosphor screen and a CMOS camera. In Fig. 5(b), the interference fringes of the fundamental (804 nm) and 13th harmonic (62 nm) are shown as function of relative intensity

Optics EXPRESS

between the pulse pair. The former is measured by taking out the XUV grating and placing the CMOS camera in the fundamental beam path, upstream of the gas-filled cell.

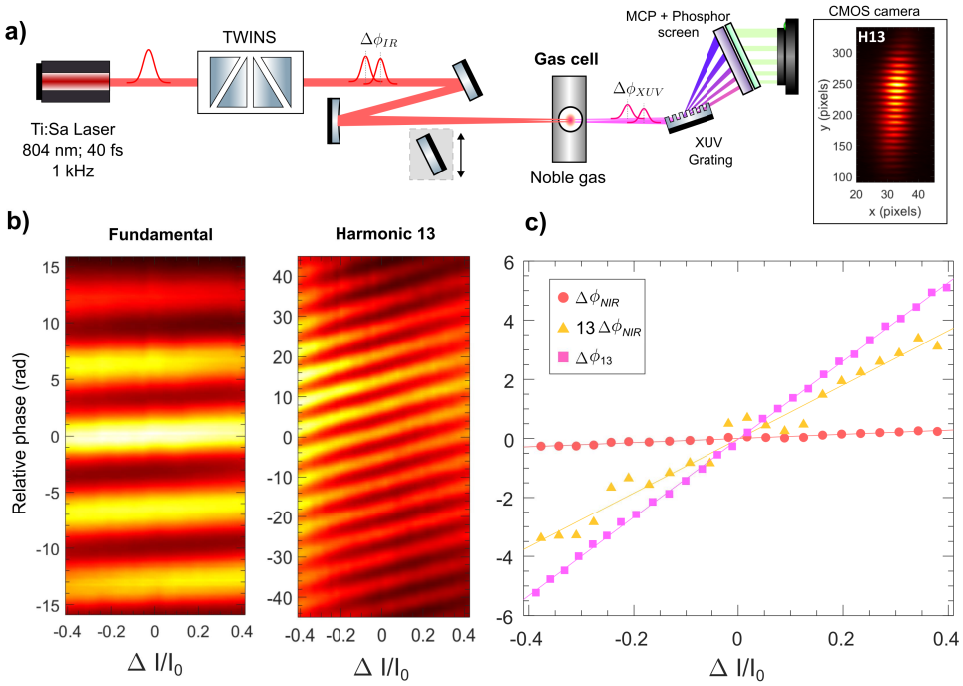

Fig. 5. (a) Schematic of the XUV interferometry setup. (b) Relative phase shift between the NIR and XUV pulse pair as function of their varying intensity ratio. (c) Comparison of the relative phase shift of the fundamental (red circles), the up converted fundamental phase shift (yellow triangles) and harmonic 13 (pink squares).

During HHG in gases, an electron is first ionized by a strong laser field and then accelerated in the continuum. Within a single half-cycle of the driving field, the electron can return to its parent ion once the field reverses direction. Upon recombination, the electron releases its accumulated kinetic energy, along with the ionization potential, as XUV radiation. Throughout this process, the oscillating dipole moment acquires a phase that is linearly dependent on the intensity of the driving field, which is in the end imparted on the generated XUV light.

Clearly the XUV interferometry measurement, as displayed in Fig. 5(a), gives direct access to the intensity dependent dipole phase. However, when only measuring the relative phase shift of the 13$^{\text{th}}$ harmonic, one would drastically overestimate the dipole contribution. Aside of the dipole phase, the harmonics are generated with a phase that is $\phi_q = q \cdot \phi_{NIR}$, where q denotes the harmonic order (in case of Fig. 5, $q = 13$) and ϕ_{NIR} is the phase of the fundamental. Any additional relative phase shift that is accumulated between the two pulses before HHG is thus multiplied by q. Figure 5(b) shows the intensity dependent relative phase shift of the fundamental and the 13$^{\text{th}}$ harmonic. The asymmetry observed in the relative phase map of harmonic 13 can be explained by a measured few percent difference in absolute peak intensity between $\Delta I/I_0 = 1$ and $\Delta I/I_0 = -1$. As stated in the Methods section, this difference is calibrated for all the shown $\Delta I/I_0$. However, due to the nonlinearity of HHG this initially small difference can have a large effect on the amplitude of the harmonic signal. Nevertheless, the linear relation between the dipole phase and intensity, as well as the linear relation between n_2 and intensity ensures that this calibrated offset does not effect the measured relative phase shift, which remains symmetric.

Optics EXPRESS

To accurately investigate the intensity dependence of the dipole phase, one must always measure the difference in B-integral of the fundamental pulses, multiply it by the harmonic order and subtract it from the measured XUV phase shift. Figure 5(c) shows the measured XUV phase shift of harmonic 13 as function of $\Delta I/I_0$ of the highest intensity fringe compared to that of the fundamental phase shift and the up-converted fundamental phase shift. Astonishingly the intensity dependent dipole phase change would be overestimated by 70% if no B-integral correction is done. Throughout the TWINS wedges the energy per pulse was 2 mJ (with a beam diameter of ~ 1 cm). After the polarizer the pulse energy was halved. Yet the intensity rises again after focusing, which, with the entrance window of the vacuum chamber (2 mm thick SiO_2, positioned halfway along the focal distance) and the gas cell (2 mm medium propagation near the focus) will add significantly to the nonlinear phase of the pulses. It is important to note that whenever the pulses are temporally and spatially overlapped, as was the case in the first ~0.5 mm of the first wedge, the last ~0.5 mm of the last wedge as well as through the entrance window, cross phase modulation between the two beams could occur when the pulses are only partially overlapped in time. For the current measurements, no clear sign of cross-phase modulation was observed as there was no shift in harmonic wavelength as function of $\Delta I/I_0$.

Detailed measurements of dipole phase in solids with a B-integral correction are provided in [19], and future work will re-investigate the dipole phase in gases in a similar manner.

4. Conclusion

As there is still a wide range of reported n_2's of a single material (sometimes deviating with factors of 2 from similar methodology [27,42]), the addition of the current method and results provide crucial data for n_2 sensitive applications. Moreover, because the common-path interferometric setup is extremely compact and stable and allows the measured sample to remain stationary, the TWINS n_2 characterization method is uniquely positioned among the existing n_2 measurement techniques. Finally, we would like to stress the importance of thorough B-integral characterization for any interferometric application of TWINS, especially when a pulse pair with unequal intensities is applied in an experiment, e.g. to drive HHG. Alongside interferometry, B-integral contributions can have impact on many recent solid-state HHG developments, such as harmonic intensity control [43–47], harmonic beam shaping and imaging [48–50], as well as super-resolution microscopy [51,52].

Funding. HORIZON EUROPE European Research Council (101041819); Nederlandse Organisatie voor Wetenschappelijk Onderzoek (VI.Vidi223.133).

Acknowledgments. We thank the mechanical workshop and the design, electronic, and software departments of ARCNL for the construction of the setup and highlight Dr. Stefan Lehman's contribution for his technical support and insight.

Disclosures. The authors declare no conflicts of interest.

Data availability. Data underlying the results presented in this paper are not publicly available at this time but may be obtained from the authors upon reasonable request.

References

1. O. Kneller, C. Mor, N. D. Klimkin, *et al.*, "Attosecond transient interferometry," Nat. Photonics **19**(2), 134–141 (2025).
2. J. C. Thiele, E. Pfitzner, and P. Kukura, "Single-protein optical holography," Nat. Photonics **18**(4), 388–395 (2024).
3. T. L. S. Collaboration, the Virgo Collaboration, the KAGRA Collaboration, "Gw231123: a binary black hole merger with total mass 190-265 $m_\odot$," arXiv (2025).
4. Z. Ludwig, "Ein neuer interferenzrefraktor," Zeitschrift für Instrumentenkunde **11**, 275–285 (1891).
5. L. Mach, "Ueber einen interferenzrefraktor," Zeitschrift für Instrumentenkunde **12**, 89 (1892).
6. J. E. Millerd, N. J. Brock, J. B. Hayes, *et al.*, "Instantaneous phase-shift point-diffraction interferometer," in *Interferometry XII: Techniques and Analysis*, vol. 5531 (SPIE, 2004), pp. 264–272.
7. G. Sagnac, "L'éther lumineux démontré par l'effet du vent relatif d'éther dans un interféromètre en rotation uniforme," CR Acad. Sci. **157**, 708–710 (1913).

Optics EXPRESS

8. Y.-C. Wang, L.-H. Shyu, and C.-P. Chang, "The comparison of environmental effects on michelson and fabry-perot interferometers utilized for the displacement measurement," Sensors **10**(4), 2577–2586 (2010).
9. K. Jeong, M. J. Lopera, J. J. Turek, *et al.*, "Common-path interferometer for digital holographic doppler spectroscopy of living biological tissues," J. Biomed. Opt. **26**(03), 030501 (2021).
10. D. Brida, C. Manzoni, and G. Cerullo, "Phase-locked pulses for two-dimensional spectroscopy by a birefringent delay line," Opt. Lett. **37**(15), 3027–3029 (2012).
11. G. Jansen, D. Rudolf, L. Freisem, *et al.*, "Spatially resolved fourier transform spectroscopy in the extreme ultraviolet," Optica **3**(10), 1122–1125 (2016).
12. A. Oriana, J. Réhault, F. Preda, *et al.*, "Scanning fourier transform spectrometer in the visible range based on birefringent wedges," J. Opt. Soc. Am. A **33**(7), 1415–1420 (2016).
13. J. Réhault, R. Borrego-Varillas, A. Oriana, *et al.*, "Fourier transform spectroscopy in the vibrational fingerprint region with a birefringent interferometer," Opt. Express **25**(4), 4403–4413 (2017).
14. A. Perri, B. Nogueira de Faria, D. T. Ferreira, *et al.*, "Hyperspectral imaging with a twins birefringent interferometer," Opt. Express **27**(11), 15956–15967 (2019).
15. F. Gucci, E. B. Molinero, M. Russo, *et al.*, "Ultrafast valleytronic logic operations," arXiv (2024).
16. D. Lesko, T. Weitz, S. Wittigschlager, *et al.*, "Tailored-light photocurrent spectroscopy for probing time-reversal symmetry-broken phases," arXiv (2025).
17. B. Ardini, F. Richter, L. Uboldi, *et al.*, "Generation of interferometrically stable pulse pairs from a free-electron laser using a birefringent interferometer," J. Phys. B: At., Mol. Opt. Phys. **57**(7), 075402 (2024).
18. J. Lu, E. F. Cunningham, Y. S. You, *et al.*, "Interferometry of dipole phase in high harmonics from solids," Nat. Photonics **13**(2), 96–100 (2019).
19. N. Kuzkova, P. J. Van Essen, B. de Keijzer, *et al.*, "Attosecond high-harmonic interferometry probes orbital- and band-dependent dipole phase in magnesium oxide," arXiv (2025).
20. R. W. Boyd, *Nonlinear Optics* (Elsevier, 2008).
21. M. Nisoli, S. De Silvestri, and O. Svelto, "Generation of high energy 10 fs pulses by a new pulse compression technique," Appl. Phys. Lett. **68**(20), 2793–2795 (1996).
22. W. H. Jabber, Q. M. Hassan, and F. Al-Saymari, "Identification of the nonlinear optical properties for a mixture of sudan yellow 3g and poly methyl methacrylate for optical limiting applications," Phys. B **669**, 415305 (2023).
23. H. G. Winful, J. Marburger, and E. Garmire, "Theory of bistability in nonlinear distributed feedback structures," Appl. Phys. Lett. **35**(5), 379–381 (1979).
24. N. Sankey, D. Prelewitz, T. Brown, *et al.*, "Optical switching dynamics of the nonlinear bragg reflector: comparison of theory and experiment," J. Appl. Phys. **73**(11), 7111–7119 (1993).
25. Q. Li, J. Song, X. Chen, *et al.*, "All-optical logic gates based on cross phase modulation effect in a phase-shifted grating," Appl. Opt. **55**(25), 6880–6886 (2016).
26. S. Mahanty and A. Kumar, "Implementation of all-optical 4 bit binary to gray code converter based on cross-phase modulation effect in a phase shifted fiber bragg grating," Opt. Quantum Electron. **54**(9), 601 (2022).
27. T. R. Ensley and N. K. Bambha, "Ultrafast nonlinear refraction measurements of infrared transmitting materials in the mid-wave infrared," Opt. Express **27**(26), 37940–37951 (2019).
28. P. Smith, W. Tomlinson, D. Eilenberger, *et al.*, "Measurement of electronic optical kerr coefficients," Opt. Lett. **6**(12), 581–583 (1981).
29. P. Maker, R. Terhune, and C. Savage, "Intensity-dependent changes in the refractive index of liquids," Phys. Rev. Lett. **12**(18), 507–509 (1964).
30. M. Miguez, E. Barbano, S. C. Zilio, *et al.*, "Accurate measurement of nonlinear ellipse rotation using a phase-sensitive method," Opt. Express **22**(21), 25530–25538 (2014).
31. Y. Ding, C. Guo, G. A. Swartzlander Jr, *et al.*, "Spectral measurement of the nonlinear refractive index in znse using self-bending of a pulsed laser beam," Opt. Lett. **15**(24), 1431–1433 (1990).
32. H. Lehmeier, W. Leupacher, and A. Penzkofer, "Nonresonant third order hyperpolarizability of rare gases and n2 determined by third harmonic generation," Opt. Commun. **56**(1), 67–72 (1985).
33. F. Kajzar and J. Messier, "Original technique for third-harmonic-generation measurements in liquids," Rev. Sci. Instrum. **58**(11), 2081–2085 (1987).
34. I. Kang, T. Krauss, and F. Wise, "Sensitive measurement of nonlinear refraction and two-photon absorption by spectrally resolved two-beam coupling," Opt. Lett. **22**(14), 1077–1079 (1997).
35. D. Milam and M. Weber, "Measurement of nonlinear refractive-index coefficients using time-resolved interferometry: application to optical materials for high-power neodymium lasers," J. Appl. Phys. **47**(6), 2497–2501 (1976).
36. I. Dancus, S. T. Popescu, and A. Petris, "Single shot interferometric method for measuring the nonlinear refractive index," Opt. Express **21**(25), 31303–31308 (2013).
37. G. Jansonas, R. Budriūnas, M. Vengris, *et al.*, "Interferometric measurements of nonlinear refractive index in the infrared spectral range," Opt. Express **30**(17), 30507–30524 (2022).
38. D. York, N. M. Evensen, M. L. Martínez, *et al.*, "Unified equations for the slope, intercept, and standard errors of the best straight line," Am. J. Phys. **72**(3), 367–375 (2004).
39. E. Nibbering, G. Grillon, M. A. Franco, *et al.*, "Determination of the inertial contribution to the nonlinear refractive index of air, n2, and o2 by use of unfocused high-intensity femtosecond laser pulses," J. Opt. Soc. Am. B **14**(3), 650–660 (1997).

Optics EXPRESS

40. D. G. Voelz, *Computational Fourier Optics: A Matlab Tutorial*, p. 51 (2011).
41. R. DeSalvo, A. A. Said, D. J. Hagan, *et al.*, "Infrared to ultraviolet measurements of two-photon absorption and n/sub 2/in wide bandgap solids," IEEE J. Quantum Electron. **32**(8), 1324–1333 (1996).
42. S. R. Flom, G. Beadie, S. S. Bayya, *et al.*, "Ultrafast Z-scan measurements of nonlinear optical constants of window materials at 772, 1030, and 1550 nm," Appl. Opt. **54**(31), F123–F128 (2015).
43. S. D. Roscam Abbing, N. Kuzkova, R. van der Linden, *et al.*, "Enhancing the efficiency of high-order harmonics with two-color non-collinear wave mixing in silica," Nat. Commun. **15**(1), 8335 (2024).
44. P. J. van Essen, Z. Nie, B. de Keijzer, *et al.*, "Toward complete all-optical intensity modulation of high-harmonic generation from solids," ACS Photonics **11**(5), 1832–1843 (2024).
45. B. De Keijzer, P. J. van Essen, and P. M. Kraus, "Effect of photoexcitation on high-harmonic generation in semiconductors," J. Opt. Soc. Am. B **41**(8), 1754–1763 (2024).
46. Z. Nie, L. Guery, E. Molinero, *et al.*, "Following the nonthermal phase transition in niobium dioxide by time-resolved harmonic spectroscopy," Phys. Rev. Lett. **131**(24), 243201 (2023).
47. C. Heide, Y. Kobayashi, A. C. Johnson, *et al.*, "Probing electron-hole coherence in strongly driven 2d materials using high-harmonic generation," Optica **9**(5), 512–516 (2022).
48. S. D. Roscam Abbing, R. Kolkowski, Z.-Y. Zhang, *et al.*, "Extreme-ultraviolet shaping and imaging by high-harmonic generation from nanostructured silica," Phys. Rev. Lett. **128**(22), 223902 (2022).
49. A. Korobenko, S. Rashid, C. Heide, *et al.*, "Generation of structured coherent extreme ultraviolet beams from an mgo crystal," Opt. Express **29**(15), 24161–24168 (2021).
50. T. Heinrich, M. Taucer, O. Kfir, *et al.*, "Chiral high-harmonic generation and spectroscopy on solid surfaces using polarization-tailored strong fields," Nat. Commun. **12**(1), 3723 (2021).
51. K. Murzyn, M. L. van der Geest, L. Guery, *et al.*, "Breaking abbe's diffraction limit with harmonic deactivation microscopy," Sci. Adv. **10**(46), eadp3056 (2024).
52. P. J. Van Essen, B. De Keijzer, T. Van Horen, *et al.*, "Spatial polarization gating of high-harmonic generation in solids," Phys. Rev. Res. **7**(1), L012063 (2025).